JOURNAL OF CATALYSIS 149, 278–291 (1994)

# $N_2O$ Reduction by CO over an Alumina-Supported Pt Catalyst: Forced Composition Cycling

Ramakant R. Sadhankar and David T. Lynch[1]

*Department of Chemical Engineering, University of Alberta, Edmonton, Alberta, Canada T6G 2G6*

Received December 7, 1993; revised May 16, 1994

**The reaction dynamics of $N_2O$ reduction by CO over an alumina-supported catalyst have been examined using forced square-wave cycling of CO and $N_2O$ concentrations. The experiments were carried out using an isothermal recycle reactor operated at 499 K with various values of the cycling frequency and the phase angle between the two composition cycles. Time-average CO conversions as high as five times the steady-state conversion were attained during the forced feed cycling. The observed dynamic behavior of the system has been described by a kinetic model consisting of three elementary steps which incorporates two main features, namely, the adsorbate-induced Pt surface-phase transformation ($1 \times 1 \leftrightarrow$ hex) and the self-exclusion of CO during adsorption on the Pt surface. The model was able to describe quantitatively the experimental results of the steady-state multiplicity behavior of the reaction. Thus, a simple model provides a consistent explanation for both the observed rate enhancement and dynamic $CO_2$ response during input cycling and the steady-state multiplicity.** © 1994 Academic Press, Inc.

## INTRODUCTION

The reduction of nitrous oxide ($N_2O$) by carbon monoxide (CO) over noble metal catalysts is an important reaction during the reduction of nitric oxide by carbon monoxide in automobile catalytic converters (1–3). In an earlier study (4), the steady-state multiplicity behavior of the $N_2O$ + CO reaction over an alumina-supported Pt catalyst was used to discriminate among several rival mechanisms. Four kinetic models were examined and it was found that only a model based on CO self-exclusion from the platinum catalyst was able to describe all of the observed behavior. However, several dissimilar sets of values of kinetic parameters produced similar model predictions, which were all in excellent agreement with the experimental data. To resolve such questions concerning kinetic models, a variety of transient response techniques have been employed. Kobayashi (5) used step changes in the feed concentration of CO and $N_2O$ to study the $N_2O$ + CO reaction over a silver catalyst. From the transient response curves of $CO_2$ and $N_2$ it was possible to distinguish between the three Hougen–Watson-type kinetic models which gave similar predictions for the steady-state experiments.

Graham and Lynch (6) used the experimental bifurcation behavior of the CO + $O_2$ reaction over a supported Pt catalyst to discriminate among several rival mechanisms. However, the proposed kinetic model based on a CO self-exclusion effect could not describe the complex reaction dynamics such as chaos and self-sustained oscillations. In a subsequent study (7), based on a transient response technique involving periodic cycling of the feed composition, a kinetic model was proposed that could describe all of the observed complex behavior of the CO + $O_2$ reaction including steady-state multiplicity, self-sustained oscillations, and rate enhancement during feed composition cycling.

In an extensive review of the periodic operation of catalytic reactors, Bailey (8) showed that the cyclic operation of catalytic reactors can lead to large improvements in reaction rate, selectivity, or both. In addition, periodic operation can be used to gain insight into the underlying reaction mechanism. The technique of square-wave cycling has been used to study both the oxidation of CO over noble metal catalysts (7, 9–17) and the NO + CO reaction (1, 3). Several of these studies (9–12) reported significant increases in the time-average reaction rate of the CO + $O_2$ reaction which could not be described by a Langmuir–Hishelwood-type reaction mechanism. Lynch (13, 14) used the forced composition cycling technique to explain the resonant behavior of CO oxidation reaction over a supported Pt catalyst. Other studies (16, 17) have used the forced cycling technique combined with infrared spectroscopy to study the underlying mechanism of CO oxidation over supported noble metal catalysts. Cho *et al.* (1) studied the reduction of NO by CO over a supported Rh catalyst during symmetric and asymmetric feed cycling experiments. They reported the formation of $N_2O$ as an important step during the CO + NO reaction. Mur-

[1] To whom correspondence should be addressed.



0021-9517/94 $6.00

aki and Fujitani (3) studied the effect of cycle period on $N_2O$ selectivity for the NO + CO reaction over a supported Pt catalyst using cycled feeds. Graham and Lynch (7) used the technique of variable phase cycling of the feed composition to study the reaction dynamics of CO oxidation over an alumina-supported Pt catalyst. They observed that variation of the phase angle between the oxygen and the CO feed cycles led to an increase in time-average conversion over and above that which occurs for the out-of-phase feed cycling. The phase angle between the two feed cycles was thus identified as an important parameter in maximizing the conversion. The technique of variable phasing of inputs during forced composition cycling was used in this study of the $N_2O$ + CO reaction. A model combining the features of CO self-exclusion and surface phase transformation (7, 18) is used to describe the experimental observations during feed cycling as well as the previously reported steady-state multiplicity behavior (4).

## METHODS

The experiments were carried out using a recycle reactor system containing 20 g of 0.5 wt% $Pt/Al_2O_3$ Engelhard catalyst. The experimental equipment and the catalyst have been previously described by Sadhankar *et al.* (4). From an earlier investigation (7) on a batch of a similar catalyst, the specific surface areas of the platinum catalyst and the alumina support were estimated to be 0.47 and 104.6 $m^2/g$, respectively, with the $CO_2$ adsorption capacity of the alumina support, $L_s$, assumed to be $1.2 \times 10^{-6}$ $mol/m^2$. The reactor pressure, temperature, and total feed flow to the reactor were always maintained at 103 kPa, 499 K, and 185 $cm^3$(STP)/min, respectively. The recycle ratio under the reactor operating conditions was estimated to be 90 from the measurement of the recycle pump flow. Under these conditions it has been found that the mixing in the recycle reactor closely approximates that of an ideal CSTR (4).

The gases used in this study were purchased from Linde and included gas mixtures of 4.99 or 10% CO in $N_2$, 10.01% $N_2O$ in $N_2$, and prepurified $N_2$. The feed compositions were in the ranges of 0–2.4% $N_2O$ and 0–2.4% CO, with nitrogen for the balance of the feed.

Four-way valves, located downstream of the mass flow controllers on the feed lines for CO and $N_2O$, were used to generate square-wave composition cycles as described by Graham and Lynch (7, 15). The time-averaged feed composition was maintained at 1.2% $N_2O$ and 1.2% CO for all of the experiments in this study. This was achieved by setting the desired flow rates of CO and $N_2O$ through the mass flow controllers and sequentially switching the downstream four-way valves between the "vent" position and the "feed" position for each half cycle as shown in Fig. 1. The square-wave cycling of the CO and $N_2O$ feed compositions did not affect the total feed flow rate to the recycle reactor, which was always maintained at 185 $cm^3$ (STP)/min by regulating the flow of makeup nitrogen. Therefore, the recycle ratio was always maintained at approximately 90 (ideal CSTR behavior) during the feed composition cycling.

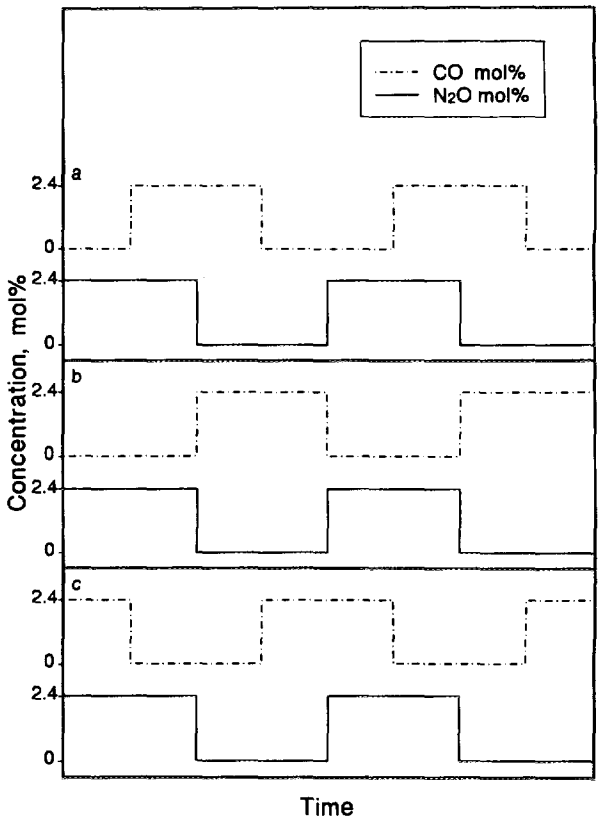


FIG. 1. Feed cycling strategies. $N_2O$ phase leads: (a) 90°, (b) 180°, and (c) 270°.

At the start of every experiment, following purging of the reactor with nitrogen, $N_2O$ was always introduced into the reactor before CO was admitted, and therefore, the $N_2O$ feed cycle has a "phase lead" over the CO feed cycle. The $N_2O$ phase lead is expressed in terms of degrees considering a complete feed cycle to contain 360°, as shown in Fig. 1, where feed cycling with $N_2O$ phase leads of 90°, 180°, and 270° are illustrated. The valve switching sequence and the cycle times could be controlled independently by digital signals from a microcomputer. Therefore, it was possible to achieve any cycle time and $N_2O$ phase lead with the experimental equipment. The frequency of cycling is defined as the inverse of the cycle period. The cycling frequencies used in this study were in the range of 0.1 to 20 mHz.

The reactor $CO_2$ and $N_2O$ concentrations were measured by Horiba infrared gas analyzer Models PIR-2000

and VIA-300, respectively. The analyzers were calibrated at the beginning of each experiment using a gas mixture (2.04% $CO_2$ in $N_2$ and 2% $N_2O$ in $N_2$) for the span calibration and $N_2$ for the zero calibration. The attainment of cycle invariance (steady-state cycling) was determined by monitoring the reactor $CO_2$ and $N_2O$ responses. In general, 10 to 30 cycles were used for each experiment. A total of 306 experiments were carried out with different combinations of the cycling frequencies and the $N_2O$ phase lead.

## RESULTS

Experiments involving feed composition cycling were carried out under isothermal conditions (499 K) with a constant total flow to the reactor so that the results could be directly compared to the results of the steady-state experiments from the earlier study (4). The steady-state CO conversion at 499 K is summarized in Fig. 2 as a function of the feed composition. The arrows in Fig. 2 indicate the bifurcation from high-to-low and low-to-high conversion steady states during the stepwise increase or decrease of the feed CO, respectively. It can be seen from Fig. 2 that a feed composition of 1.2% CO and 1.2% $N_2O$ is in the unique low conversion region to the right of the multiplicity region. The steady-state CO conversion under these conditions was 20%.

In the first set of experiments, the CO and $N_2O$ feed cycles were out-of-phase with each other, with $N_2O$ phase lead of 180°. Therefore, the feed concentration alternated between 0% CO and 2.4% $N_2O$ for the first half-cycle to 2.4% CO and 0% $N_2O$ for the second half-cycle. The $CO_2$ response and the time-average CO conversions were determined for the out-of-phase cycling over a frequency range of 0.7 to 20 mHz. In the second part of the study, the effect of $N_2O$ phase leads of 90° and 270°, respectively,

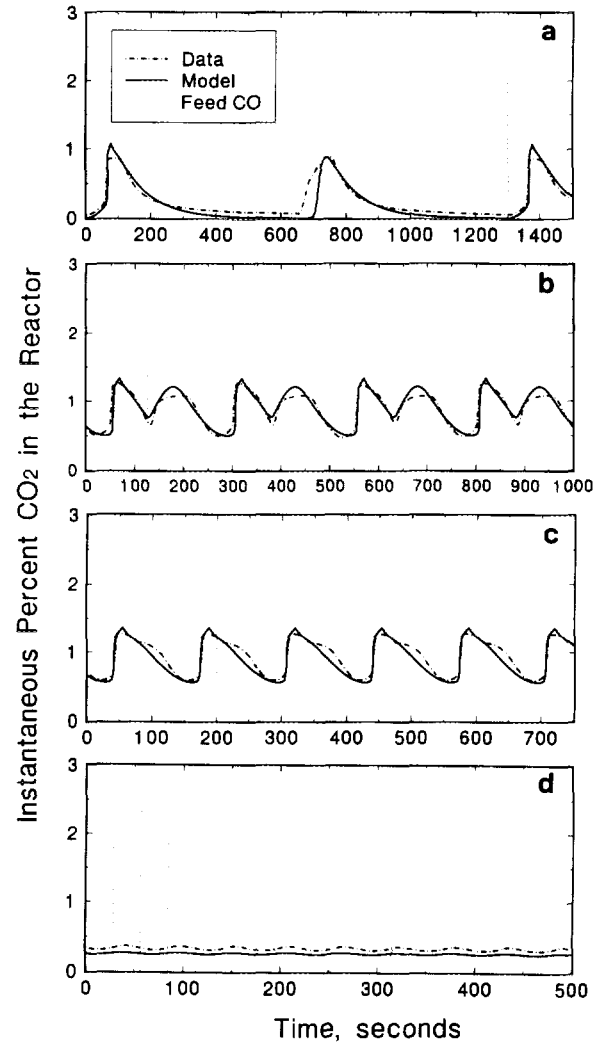


FIG. 3. Dynamic $CO_2$ response during 180° out-of-phase feed composition cycling. (a) $\omega$ = 0.77 mHz, (b) $\omega$ = 3.99 mHz, (c) $\omega$ = 7.51 mHz, (d) $\omega$ = 17.76 mHz.

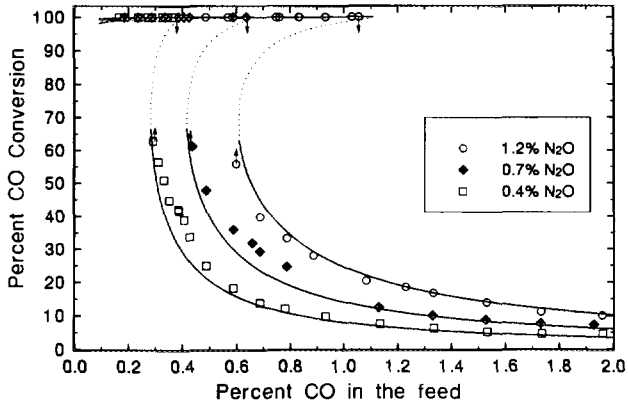


FIG. 2. Multiplicity behavior during the reduction of $N_2O$ by CO at 499 K. (—) model predictions, (···) unstable steady state predicted by the model.

on the time-average CO conversion was studied over a frequency range of 0.1 to 20 mHz. In the third part of the study, the experiments were carried out at a fixed cycling frequency and the effect of $N_2O$ phase lead on the time-average CO conversion was studied. The experiments were repeated for five different cycling frequencies.

### *Out-of-Phase Cycling*

The dynamic $CO_2$ response during out-of-phase cycling is shown by the dashed lines in Fig. 3. At a low cycling frequency of 0.77 mHz (Fig. 3a), the $CO_2$ concentration increased slowly after the $N_2O$ was switched on. At the beginning of the $N_2O$ half-cycle, the catalyst surface is saturated with adsorbed CO from the previous CO half-cycle. The gas-phase CO concentration is also very close

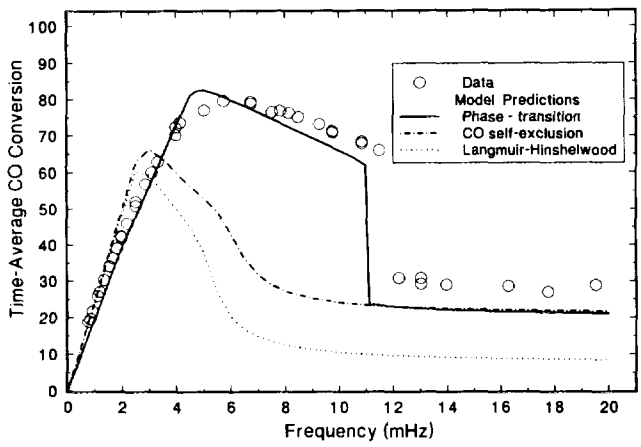


FIG. 4. Comparison of model predictions to experimental data of time-average conversion for out-of-phase cycling. $N_2O$ phase lead = 180°.

to 2.4% at the start of the $N_2O$ half-cycle. Due to the lack of empty sites for $N_2O$ dissociation, the surface reaction does not proceed to any appreciable extent. This observation is also consistent with the experimental finding that a unique low conversion steady state was obtained for high feed CO concentrations (Fig. 2). As the gas-phase CO is depleted via transport out of the reactor, more active sites become available on the catalyst surface for $N_2O$ dissociative adsorption. When sufficient active surface sites are available for $N_2O$ dissociation, the $CO_2$ concentration rises rapidly and reaches a peak value. The reactor $CO_2$ concentration then decreases as the gas-phase CO is depleted and the adsorbed CO is removed by reaction. The catalyst then becomes covered with adsorbed oxygen by the end of the $N_2O$ half-cycle.

When CO is switched on, and $N_2O$ is switched off, the $CO_2$ concentration increases rapidly. The CO entering the reactor readily reacts with the adsorbed oxygen. After the gas-phase $N_2O$ is completely depleted, the $CO_2$ concentration drops almost exponentially as the CO cleans the catalyst surface of the remaining adsorbed oxygen. The surface then becomes saturated with adsorbed CO at the end of the CO half-cycle. Typically, two peaks in $CO_2$ concentration, one in each half-cycle, were observed for frequencies lower than 5 mHz. The $CO_2$ response at the cycling frequency of 3.99 mHz is shown in Fig. 3b. A comparison of Figs. 3a and 3b shows that the time-average $CO_2$ concentration at a frequency of 3.99 mHz is higher than that at a frequency of 0.77 mHz. An almost linear relationship between the time-average $CO_2$ concentration and the cycling frequency was observed for frequencies lower than 4 mHz. The $CO_2$ concentration does not fall to zero during the long cycles (Fig. 3a) because of the $CO_2$ desorption from the alumina support.

As the frequency is increased above 5 mHz, the two peaks in $CO_2$ concentration per feed cycle began to merge, resulting in a single maximum per cycle as shown in Fig. 3c for a cycling frequency of 7.51 mHz. The magnitude of the $CO_2$ response to the feed cycling decreased as the frequency was further increased until, as can be seen in Fig. 3d, at a cycling frequency of 17.76 mHz, the time-average $CO_2$ concentration was approximately equal to the steady-state value.

The time-average CO conversions for the out-of-phase cycling experiments were calculated from the $CO_2$ response curves and are given in Fig. 4. It is seen that the CO conversion increased almost linearly with increasing frequency up to 4 mHz. This can be explained in a manner similar to that which was used to explain the CO conversion for the CO + $O_2$ reaction during out-of-phase cycling by Graham and Lynch (7). At low frequencies, two peaks of $CO_2$ concentration per cycle (Fig. 3a) were observed and the areas under the curves for each half-cycle were approximately equal. The $CO_2$ production in each half-cycle can be approximately estimated by considering the surface reaction of a monolayer of adsorbed species (CO or oxygen) plus complete reaction of one reactor volume of gas phase species (CO or $N_2O$). The total $CO_2$ production per cycle is almost constant for all of the low frequencies. Because the CO feed per cycle is equal, CO conversion is linearly proportional to the frequency of cycling. Thus, the time-average CO conversion at low frequencies can be estimated by

$$f_{TA} = \frac{(2a_m L_m + 2V[N_2O]_0)}{Q_0[CO]_0} 100\omega\%. \qquad [1]$$

A comparison of the prediction of time-average CO conversion from Eq. [1] with the experimental data is presented in Fig. 5 for frequencies up to 2.5 mHz. As can

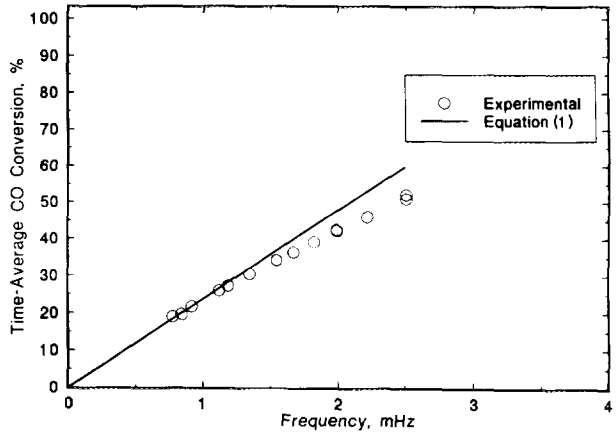


FIG. 5. Comparison of predictions of time-average conversion from Eq. [1] to experimental data for low-frequency out-of-phase cycling. $N_2O$ phase lead = 180°.

be seen from Fig. 5, the predictions match the experimental results for frequencies lower than 1.25 mHz. However, the predicted conversion from Eq. [1] is higher than the experimental values for frequencies above 2.5 mHz due to the incomplete saturation of the surface at the higher frequencies.

As can be seen from Fig. 4, the highest CO conversion of 79.5% was obtained at a frequency of 6.7 mHz, and it is approximately four times the steady-state conversion. As the frequency exceeded approximately 12 mHz, the time-average CO conversion abruptly dropped to a low value of 28%. At high frequencies, the gas-phase CO and $N_2O$ concentrations are always in the region of feed compositions which give low conversion steady states (Fig. 2). The gas-phase CO concentration does not deplete significantly even by the end of the $N_2O$ half-cycle, and therefore the catalyst surface is always highly covered with adsorbed CO during high-frequency feed cycling, which leads to a low time-average CO conversion. The critical frequency at which a transition in the time-average CO conversion occurs from a high value to a low value can be estimated from the steady-state bifurcation behavior of the reaction, as demonstrated elsewhere (7). The critical frequency for these out-of-phase cycling experiments lies between 11.5 and 12.2 mHz.

### *$N_2O$ Phase Leads of 90° and 270°*

In the second part of the study, the experiments were carried out with $N_2O$ phase leads of 90° and 270°, respectively, over a cycling frequency range of 0.1 to 20 mHz. The $N_2O$ phase lead of 270° is equivalent to a CO phase lead of 90°. The time-average CO conversions are summarized in Fig. 6. For the frequencies lower than 8 mHz, the time-average CO conversions for feed cycling with a 90° $N_2O$ phase lead were generally higher than those observed for a 270° $N_2O$ phase lead.

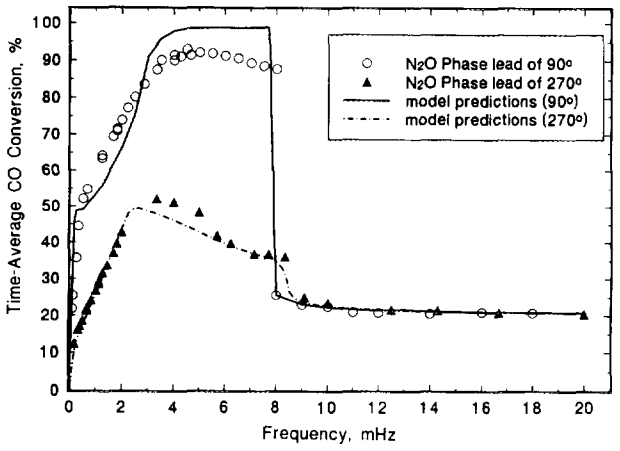


FIG. 6. Effect of cycling frequency on time-average CO conversion for $N_2O$ phase leads of 90° and 270°.

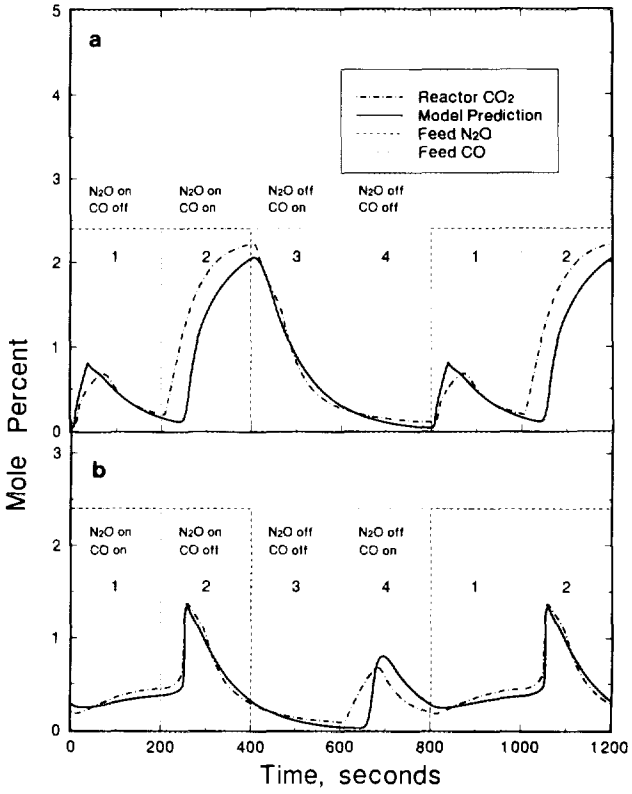


FIG. 7. Dynamic $CO_2$ response for (a) 90° and (b) 270° $N_2O$ phase leads. $\omega$ = 1.25 mHz.

For the 90° $N_2O$ phase lead cycling, the time-average CO conversion rose rapidly with increasing frequency up to 0.25 mHz. At frequencies between 0.25 and 3 mHz, the time-average CO conversion was approximately proportional to the cycling frequency. The highest time-average conversion of 93% was obtained at a frequency of 4.5 mHz, although a value of approximately 90% was found over the entire frequency range of 4 to 6.5 mHz within the accuracy of measurement. At a critical frequency of 8 mHz, the time-average CO conversion dropped abruptly from 88 to 25.4%.

For the feed cycling with an $N_2O$ phase lead of 270°, a linear relationship between the cycling frequency and the time-average CO conversion was observed over the frequency range of 0.2 to 2 mHz. The highest conversion of 52% was obtained at a frequency of 3.33 mHz for the feed cycling with 270° $N_2O$ phase lead. In the critical frequency range, the conversion dropped from 36% at 8.33 mHz to 25% at 9.1 mHz. A comparison of Fig. 4 and Fig. 6 shows that the highest CO conversion for an $N_2O$ phase lead of 180° lies between the highest CO conversions obtained for 90° (93%) and 270° (52%) $N_2O$ phase leads, respectively.

The $CO_2$ response curves at a frequency of 1.25 mHz are shown by the dashed lines in Fig. 7 for feed cycling with $N_2O$ phase leads of 90° and 270°, respectively. An

examination of these $CO_2$ response curves in Fig. 7 provides an explanation for high CO conversions obtained for 90° $N_2O$ phase lead cycling. A comparison of Figs. 7a and 7b shows that both cycles can be divided into four quadrants, each with feed containing only CO, both CO and $N_2O$, only $N_2O$, and no CO or $N_2O$ (blank feed), respectively, although the sequence of these quadrants is different for Figs. 7a and 7b. For 90° $N_2O$ phase lead cycling, the feed containing only $N_2O$ in the first quadrant removes the residual adsorbed CO from the previous blank-feed cycle, and therefore the $CO_2$ production in the first quadrant is limited. The surface is saturated with oxygen by the end of the first quadrant. In the second quadrant of the cycle, the feed CO readily adsorbs on the surface saturated with adsorbed oxygen and a high reaction rate is obtained. Almost 50% of the total $CO_2$ production occurs in the second quadrant of the cycle. In the third quadrant, the feed containing only CO reacts with the residual $N_2O$ from the previous quadrant. The reaction rate decreases as the $N_2O$ is depleted. By the end of the third quadrant, the surface is again saturated with adsorbed CO. In the fourth quadrant, the $CO_2$ desorbs from the alumina support. Some of the adsorbed CO also desorbs in the fourth quadrant due to the very low partial pressure of CO in the reactor. Therefore, the $CO_2$ production in the first quadrant is limited due to the residual adsorbed CO.

When the feed is cycled with an $N_2O$ phase lead of 270°, the first quadrant of the cycle has a feed containing both CO and $N_2O$. However, the $CO_2$ production is very small. This is because the catalyst surface is saturated with adsorbed CO from the previous (fourth) quadrant with CO-only feed. Therefore, for a sufficiently long cycle, the CO conversion in this quadrant will be equal to the steady-state conversion of 20%. In the second quadrant, when CO is switched off (feed containing only $N_2O$), the gas-phase $N_2O$ does not readily dissociate on the CO-saturated catalyst surface. As the adsorbed CO gradually reacts, sufficient active sites become available for $N_2O$ dissociation and the reaction rate increases rapidly as evident by a sharp $CO_2$ peak in this quadrant. The catalyst surface is covered by adsorbed oxygen by the end of the second quadrant. In the third quadrant, the feed does not contain either CO or $N_2O$, and therefore the $CO_2$ production is mainly due to desorption from the alumina support. In the fourth quadrant, the feed contains only CO which reacts with the residual adsorbed oxygen from the previous quadrant. The $CO_2$ production is limited by the amount of residual adsorbed oxygen at the beginning of the fourth quadrant.

The main difference between Figs. 7a and 7b is the $CO_2$ production in the overlap quadrant of the cycle with feed containing both CO and $N_2O$. The catalyst surface is saturated with adsorbed oxygen at the beginning of the overlap quadrant for an $N_2O$ phase lead of 90° and a high reaction rate is obtained. On the other hand, the catalyst surface is saturated with adsorbed CO at the beginning of the overlap quadrant for an $N_2O$ phase lead of 270° and this leads to a low reaction rate. A very similar phenomenon was observed at other frequencies lower than 7.7 mHz. It can therefore be generalized that, for frequencies lower than the critical frequency, the time-average CO conversion for $N_2O$ phase leads of less than 180° will be higher than that for $N_2O$ phase leads of greater than 180°.

### *Variable Phasing of Inputs*

In the earlier experiments, the effect of cycling frequency on the time-average CO conversion was studied for three values of $N_2O$ phase lead of 180, 90, and 270°, respectively. To determine the effect of phase angle on the time-average conversion, the experiments were carried out by varying the $N_2O$ phase lead between 0° and 360° while holding the cycling frequency constant. The results of the experiments carried out at five different frequencies are summarized in Fig. 8.

At a low frequency of 2 mHz (Fig. 8a), the time-average CO conversion increased rapidly with increasing $N_2O$ phase lead between 10° and 40°. The highest CO conversion of 93.5% was obtained at a 40° phase lead. The time-average CO conversion then decreased with increasing $N_2O$ phase leads between 50° and 180°. The time-average conversion was approximately constant at 42% over the range of phase leads between 180° and 300°. The conversions in the range of phase leads of 180° and 300° can also be estimated by Eq. [1] without significant error, as demonstrated for the out-of-phase cycling in Fig. 5. The time-average conversions decreased sharply as the phase lead was increased above 310°. The experimental observations in Fig. 8a also support the earlier generalization that relatively high time-average conversions are obtained for $N_2O$ phase leads of less than 180°.

For feed cycling at 5 mHz, as shown in Fig. 8b, the time-average CO conversion was approximately equal to its steady-state value of 20% at small phase-leads of 10° to 20° and then rose sharply as the phase-lead was increased to 45°. A high time-average conversion between 80 and 92.5% was attained over a wide range of phase leads of 50° to 180°. An increase in phase lead above 180° caused the time-average conversion to drop gradually and eventually reached its steady-state value for phase leads of 320° to 360°. A very similar behavior was also observed at a cycling frequency of 7.04 mHz (Fig. 8c) except that the span of phase leads over which high conversions were obtained was narrower than that encountered at 5 mHz. The other significant difference between Figs. 8b and 8c is that the size of the regions of near-steady-state conversion increased as the frequency increased. As the frequency

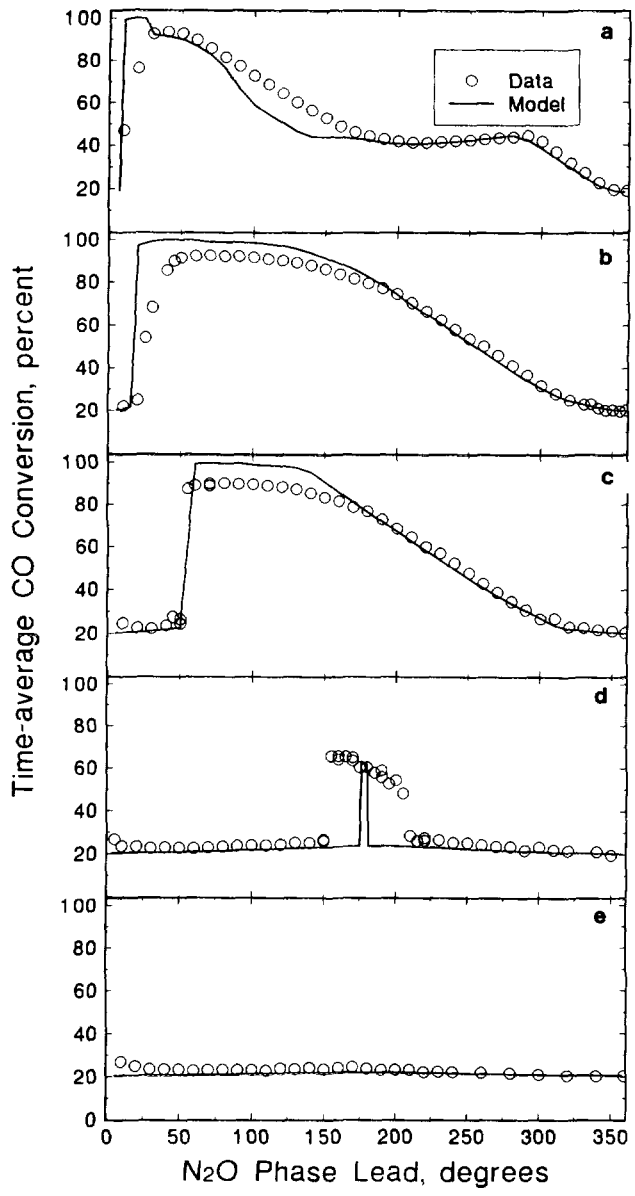


FIG. 8. Effect of $N_2O$ phase lead on the time-average conversion during cycling. (a) $\omega$ = 2 mHz, (b) $\omega$ = 5 mHz, (c) $\omega$ = 7.04 mHz, (d) $\omega$ = 11.11 mHz, (e) $\omega$ = 15.15 mHz.

was increased further to 11.11 mHz (Fig. 8d), the rate enhancement was obtained only for a narrow range of phase leads (155° to 205°). For a high frequency of 15.15 mHz, the time-average conversion was approximately equal to its steady-state value for all phase leads as shown in Fig. 8e.

The $CO_2$ response curves for a cycling frequency of 5 mHz at five different $N_2O$ phase leads are shown by dashed lines in Fig. 9. For phase-leads of 10° and 330°, there is a significant overlap of CO and $N_2O$ feed cycles, so that the gas-phase composition in the reactor is always in the low conversion region (Fig. 2) characterized by a catalyst surface saturated with adsorbed CO. Therefore, the low reaction rates result in relatively flat $CO_2$ curves, as shown in Figs. 9a and 9e. For phase-leads of 50° and 130°, sufficient time is available for reacting away most of the adsorbed CO and the catalyst surface is saturated by adsorbed oxygen before the CO and $N_2O$ feed cycles overlap. Therefore, high reaction rates are obtained in the region of CO and $N_2O$ overlap, as characterized by the large peaks of $CO_2$ in Figs. 9b and 9c. A comparison of Figs. 9c and 9d shows that the major $CO_2$ peak occurs

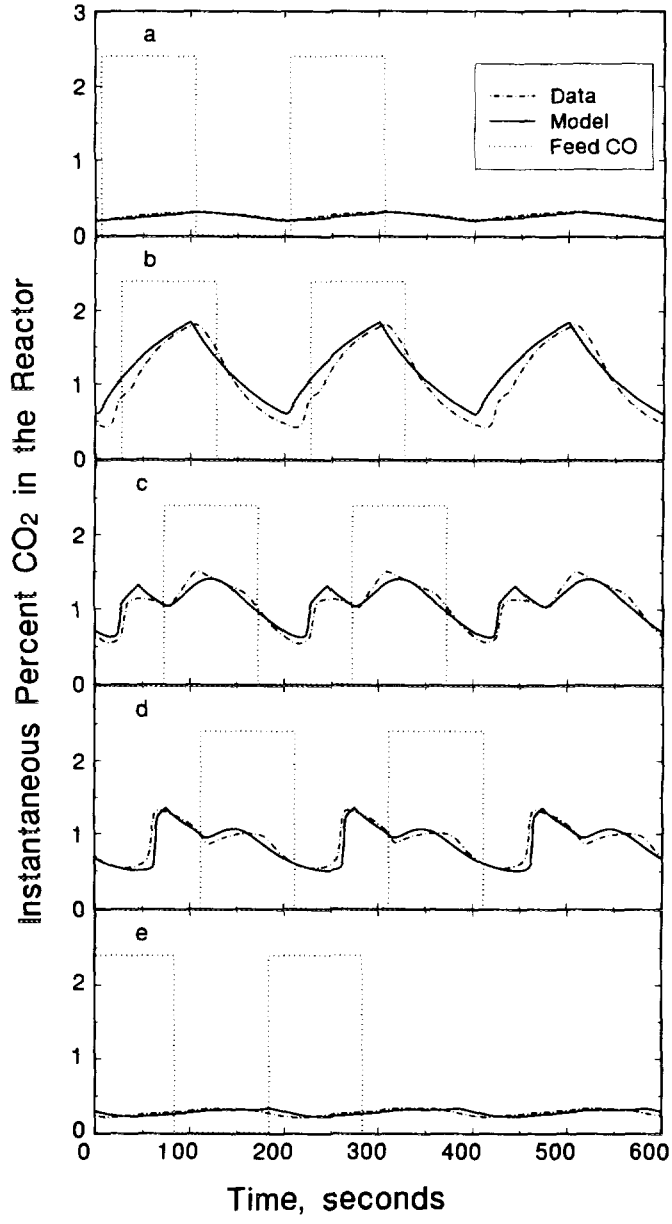


FIG. 9. Effect of $N_2O$ phase-lead on the dynamic $CO_2$ response for $\omega$ = 5 mHz. (a) $N_2O$ phase lead = 10°, (b) $N_2O$ phase lead = 50°, (c) $N_2O$ phase lead = 130°, (d) $N_2O$ phase lead = 200°, (e) $N_2O$ phase lead = 330°.

in the CO–$N_2O$ overlap part of the cycle for 130° phase lead and in the $N_2O$-only part of the cycle for 200° phase lead. The differences between Figs. 9c and 9d are very similar to the differences in Figs. 7a and 7b, for which an explanation was given earlier.

From these experiments it is apparent that the maximum time-average conversion can be obtained for an appropriate combination of $N_2O$ phase lead (less than 180°) and cycling frequency. In this study the highest time-average CO conversion of 93.5% was attained at a frequency of 2 mHz with an $N_2O$ phase lead of 40°. In general, a certain overlap of the CO and $N_2O$ cycles gives a time-average conversion which is higher than the highest conversion obtained for the out-of-phase cycling, particularly for the intermediate frequency range of 2 to 7 mHz. These observations are consistent with the findings of Graham and Lynch for the CO + $O_2$ reaction (7).

*Mathematical Model*

A mathematical model for the reaction processes must be able to describe the dynamic behavior of the reaction and the rate enhancements observed in this study as well as the steady-state multiplicity observed in the earlier study (4). As a starting point, the steady-state model which was earlier used to describe the multiplicity behavior was recast in a dynamic form to determine if description of the reaction dynamics was possible.

*CO Self-Exclusion Model*

In the earlier study (4), the steady-state multiplicity of the $N_2O$ + CO reaction over an alumina-supported Pt catalyst was described by a model incorporating carbon monoxide self-exclusion from the platinum surface. The proposed reaction mechanism consisted of the following three elementary steps:

$$CO(g) + M \rightleftarrows CO\text{–}M \quad [2]$$

$$N_2O(g) + M \rightarrow N_2(g) + O\text{–}M \quad [3]$$

$$CO\text{–}M + O\text{–}M \rightarrow CO_2(g) + 2M. \quad [4]$$

It was shown that the CO self-exclusion effect could describe the experimental low-conversion steady-state results. The CO self-exclusion effect requires that an adsorbed CO molecule exclude other CO molecules from an area equivalent in size to $N_{CO}$ surface Pt atoms, where $N_{CO}$ is slightly greater than unity.

The reactor used in this study can be modeled as an isothermal CSTR due to the high recycle ratio that was employed. As previously shown (4), the internal diffusion and external mass transfer resistances are negligible under the experimental conditions used in this study. Thus, mass balances on the gas-phase and surface species produce the following six dimensionless ordinary differential equations, where all symbols are defined under Notation:

$$\frac{dX}{d\tau} = X_0 - Q_n X - K_1 X(1 - \theta_{CO} - \theta_O)\frac{(1 - N_{CO}\theta_{CO})}{(1 - \theta_{CO})} + K_{-1}\theta_{CO} \quad [5]$$

$$\frac{dY}{d\tau} = Y_0 - Q_n Y - K_2 Y(1 - \theta_{CO} - \theta_O) \quad [6]$$

$$\frac{dZ}{d\tau} = Z_0 - Q_n Z + K_3\theta_{CO}\theta_O - K_4 Z(1 - \xi_{CO_2}) + K_{-4}\xi_{CO_2} \quad [7]$$

$$\frac{d\theta_{CO}}{d\tau} = \alpha_m\left[K_1 X(1 - \theta_{CO} - \theta_O)\frac{(1 - N_{CO}\theta_{CO})}{(1 - \theta_{CO})} - K_{-1}\theta_{CO} - K_3\theta_{CO}\theta_O\right] \quad [8]$$

$$\frac{d\theta_O}{d\tau} = \alpha_m\left[\frac{F_{N_2O}}{F_{CO}} K_2 Y(1 - \theta_{CO} - \theta_O) - K_3\theta_{CO}\theta_O\right] \quad [9]$$

$$\frac{d\xi_{CO_2}}{d\tau} = \alpha_S[K_4 Z(1 - \xi_{CO_2}) - K_{-4}\xi_{CO_2}], \quad [10]$$

where

$$Q_n = 1 - F_{CO}\left[K_1 X(1 - \theta_{CO} - \theta_O)\frac{(1 - N_{CO}\theta_{CO})}{(1 - \theta_{CO})} - K_{-1}\theta_{CO} - K_3\theta_{CO}\theta_O + K_4 Z(1 - \xi_{CO_2}) - K_{-4}\xi_{CO_2}\right]. \quad [11]$$

Equations [5] to [10] can be used to describe the steady-state behavior by setting the time derivatives in the equations to zero and solving the resulting algebraic equations. For steady-state operation, $X_0 = 1$, $Y_0 = 1$, and $Q_n = 1$, and in addition $Z_0 = 0$ for all conditions because $CO_2$ was not present in the feed. The values of the kinetic parameters $K_1$, $K_{-1}$, $K_2$, and $K_3$ must be selected so as to describe all of the time-average CO conversions during cycling experiments as well as the steady-state multiplicity data from the earlier experimental study (4). The time-average CO conversion is not affected by the adsorption and desorption of $CO_2$ on the alumina support. Therefore, in initial attempts to determine appropriate values of the kinetic parameters, the values of the $CO_2$ adsorption and desorption rate constants $K_4$ and $K_{-4}$ were set equal to zero while time-average CO conversions were calculated. Further simplification of the model was made by setting $Q_n$ equal to unity because of the low values of the gas-phase concentrations used in this study. The set of five differential equations [5]–[9] was integrated over several cycles, using a variable-step-size fourth-order Runge–

Kutta–Fehelberg method to calculate the time-average CO conversion during feed composition cycling.

Integration was always performed using the initial conditions $X = Y = Z = \theta_{CO} = \theta_O = 0$. During composition cycling, the dimensionless feed concentrations of CO and $N_2O$, $X_0$ and $Y_0$, respectively, have values of either 2 or 0, as given by the following conditions for the $n$th cycle:

for all values of $\phi_{N_2O}$

$$Y_0 = 2, \quad (n-1)\tau_C \le \tau < \left(n - \frac{1}{2}\right)\tau_C \qquad [12]$$

$$Y_0 = 0, \quad \left(n - \frac{1}{2}\right)\tau_C \le \tau < n\tau_C, \qquad [13]$$

for $0° \le \phi_{N_2O} < 180°$

$$X_0 = 0, \quad (n-1)\tau_C \le \tau < \left(n - 1 + \frac{\phi_{N_2O}}{360}\right)\tau_C \qquad [14]$$

$$X_0 = 2, \quad \left(n - 1 + \frac{\phi_{N_2O}}{360}\right)\tau_C \le \tau < \left(n - \frac{1}{2} + \frac{\phi_{N_2O}}{360}\right)\tau_C \qquad [15]$$

$$X_0 = 0, \quad \left(n - \frac{1}{2} + \frac{\phi_{N_2O}}{360}\right)\tau_C \le \tau < n\tau_C, \qquad [16]$$

for $180° \le \phi_{N_2O} < 360°$

$$X_0 = 2, \quad (n-1)\tau_C \le \tau < \left(n - \frac{3}{2} + \frac{\phi_{N_2O}}{360}\right)\tau_C \qquad [17]$$

$$X_0 = 0, \quad \left(n - \frac{3}{2} + \frac{\phi_{N_2O}}{360}\right)\tau_C \le \tau < \left(n - 1 + \frac{\phi_{N_2O}}{360}\right)\tau_C \qquad [18]$$

$$X_0 = 2, \quad \left(n - 1 + \frac{\phi_{N_2O}}{360}\right)\tau_C \le \tau < n\tau_C. \qquad [19]$$

The attainment of cycle invariance was determined according to the procedures described by Graham and Lynch (7). When several sequential integrations were performed, i.e., $\omega$ varied, $\phi_{N_2O}$ varied, etc., the initial conditions for successive integrations were based on the final state of the immediately preceding converged cycle.

The initial estimates of the kinetic parameters were obtained from the values used to describe the steady-state multiplicity behavior (4). It was found that the model predictions for time-average CO conversion for the feed cycling were considerably lower than the experimental data. The model predictions for time-average CO conversions for feed cycling could be improved by increasing the values of rate parameters $K_2$ and $K_3$. However, increasing the values of $K_2$ and $K_3$ necessitated the change of other parameters in order to maintain agreement with the steady-state data. In particular, it was necessary to reduce the value of the CO self-exclusion factor, $N_{CO}$, in order to be able to describe the experimental low conversion steady-state data and the low-to-high conversion bifurcation points for high values of $K_2$ and $K_3$. However, the large values of $K_2$ and $K_3$ also resulted in significant model–experimental discrepancies in the values of feed CO% at which high-to-low conversion bifurcation occurs for steady-state experiments. While maintaining a complete model–experimental agreement for the steady-state data, it was possible to vary the values of $K_2$ and $K_3$ only marginally when attempting to improve the predictions of the time-average CO conversions during feed cycling. Over large regions of parameter space, the values of the CO adsorption and desorption rate parameters, $K_1$ and $K_{-1}$, did not have any significant effect on model predictions as long as the ratio of $K_1$ to $K_{-1}$ was maintained constant. The main effect of lower values of $K_1$ and $K_{-1}$ was a reduction in the number of integration steps needed to solve the differential equations. Therefore, in order to prevent the computational requirements from becoming unmanageable, relatively low values of $K_1$ and $K_{-1}$ (while holding the ratio constant) were always used. A low value of $K_1$ implies a correspondingly low value of the CO sticking probability, $S_{CO}$. It is possible to increase arbitrarily the value of $S_{CO}$ by one or more orders of magnitude (with a corresponding increase in $k^0_{-1}$ to keep $K_1/K_{-1}$ constant) without significantly affecting the predictions from the model.

The predictions of the time-average CO conversion for out-of-phase feed cycling from the CO self-exclusion model are shown by the dashed line in Fig. 4, where it can be seen that the model predictions approximately match the experimental data at frequencies below 3 mHz and at high frequencies above 11 mHz. The values of the kinetic parameters are listed in Table 1. As discussed earlier, the time-average conversion for the low frequencies can be estimated reasonably accurately by Eq. [1] and, therefore, is relatively insensitive to the reaction mechanism model. However, the model predictions are consistently lower than the experimental data for the intermediate frequency range of 3 to 11 mHz. The effect of CO self-exclusion is illustrated by setting $N_{CO}$ equal to unity as shown by the dotted line in Fig. 4. As can be seen from Fig. 4, the time-average CO conversions predicted from a Langmuir–Hinshelwood-type model ($N_{CO} = 1$) are consistently lower than those predicted by

TABLE 1

Kinetic Parameters

| | CO self-exclusion model | Surface-phase transformation model |
|---|---|---|
| $K_1$ (499 K) | 28,000 | 28,000 |
| $K_{-1}$ (499 K, 1% CO feed) | 100 | 15.75 |
| $K_2$ (499 K) | 18 | 23.6 |
| $K_3$ (499 K, 1% CO feed) | 20 | 20 |
| $k_{-1}^0$ | $6.314 \times 10^3$ | $6.298 \times 10^4$ |
| $k_2^0$ | $4.8415 \times 10^8$ | $4.0624 \times 10^8$ |
| $k_3^0$ | $5.3213 \times 10^{11}$ | $5.2355 \times 10^{14}$ |
| $E_{-1}$ | 36.84 | 52.77 |
| $E_2$ | 85.77 | 72.77 |
| $E_3$ | 74.34 | 100.03 |
| $S_{CO}$ | $1.076 \times 10^{-4}$ | $1.076 \times 10^{-4}$ |
| $L_m$ | $2 \times 10^{-5}$ | $1.42 \times 10^{-5}$ |
| $N_{CO}$ | 1.018 | 1.0015 |

the CO self-exclusion model, particularly for frequencies higher than 11 mHz. This observation is consistent with the earlier study (4) where only the CO self-exclusion effect could account for the experimentally observed CO conversions for the unique low-conversion steady state. Therefore, CO self-exclusion was considered as an integral part of further model development. In order to describe the high values of time-average conversion during feed cycling experiments, as well as the steady-state multiplicity, it was necessary to use a surface-phase transformation model similar to that described by Lynch (18) and Graham and Lynch (7).

*Surface-Phase Transformation Model*

It has been shown that a clean Pt(100) surface undergoes a reconstruction from a quadratic (1 × 1) structure to quasihexagonal order corresponding to a complicated (5 × 20) LEED pattern (19) which appears to be the thermodynamically favored structure (20). Numerous studies (21–26) have shown that the reconstruction [(5 × 20) LEED pattern] exhibited by the clean Pt(100) surface is removed by the adsorbate-induced interaction of CO, $O_2$, $H_2$, or NO. Thiel *et al.* (27) observed that the nucleation of (1 × 1) patches occurs on the reconstructed (hex) surface of Pt(100) even at a very low CO surface coverage and proceeds until the entire surface has been converted to the (1 × 1) phase at $\theta_{CO} = 0.5$. On the other hand, during CO desorption, the hex phase does not return until the fractional CO surface coverage is decreased below 0.3. The reconstructed surface (hex phase) is less active than the unreconstructed (1 × 1) surface. The oxygen sticking probability is low for the surface in the hex phase (26), but is at least two orders of magnitude larger for the (1 × 1) surface (28). A similar observation is reported by Bonzel *et al.* (29) for NO adsorption on Pt(100). They observed no adsorption of NO on the reconstructed hex surface at temperatures higher than 380 K. On the other hand, the unreconstructed (1 × 1) surfaces were able to adsorb NO molecularly up to temperatures of 410 K.

The phenomenon of the adsorbate-induced reversible surface-phase transition for the clean Pt(100) surface and resulting reaction rate enhancements have been used to describe the kinetic oscillations of the CO + $O_2$ reaction (30) and the NO + CO reaction (31, 32) under high vacuum conditions on well-characterized catalyst surfaces. However, to describe the rate oscillations of CO oxidation on supported Pt catalyst and Pt foils at near atmospheric pressure, various other mechanisms have been proposed. For example, a process of slow oxidation and reduction of the catalyst surface (33, 34) has been used to model the rate oscillations of CO oxidation on Pt at atmospheric pressure. It has also been suggested (35) that the formation of platinum oxide is catalyzed by silicon impurities on the supported catalyst. Other studies (36, 37) proposed that a process of slow activation/deactivation of the catalyst surface due to diffusion of carbon to the surface may be responsible for observed oscillations of CO oxidation on Pt foil at atmospheric pressure. A kinetic model based on the variation of the catalyst surface temperature (38) has also been suggested to describe the self-sustained oscillations of CO oxidation on silica-supported Pt pellets at atmospheric pressure. Nevertheless, the Pt(100) surface transformation phenomenon has been successfully used (18) to describe the self-sustained oscillations of CO oxidation on alumina-supported Pt catalyst at atmospheric pressure. A similar mechanism has also been suggested (39) for oscillations of NO + CO reaction on polycrystalline Pt–$Al_2O_3$ catalyst in FTIR spectroscopic investigations. Schwartz and Schmidt (31) suggested that the adsorbate-induced (1 × 1) ↔ hex surface-phase transition may be operative on supported Pt catalysts because in many reactive gases all crystallographic orientations tend to facet into predominantly (100) crystal planes. Wang *et al.* (40) have shown that supported platinum crystallites form predominantly (100) crystal planes when grown in hydrogen. These studies lend support to the model based on Pt(100) surface-phase transition to describe the rate oscillations on supported Pt catalyst. Graham and Lynch (7) used the surface-phase transformation effect to describe the complex behavior, including steady-state multiplicity and reaction rate enhancement during feed cycling, of the CO + $O_2$ reaction on an alumina-supported Pt catalyst at atmospheric pressure. Because of the apparent similarity of the CO + $N_2O$ and CO + $O_2$ reaction systems, the same surface-phase transformation phenomenon has been used in this study to describe the reaction rate enhancement for the CO + $N_2O$ reaction during feed cycling.

As shown by Graham and Lynch (7), the use of the surface-phase transformation model requires that the rate constants for oxygen adsorption and surface reaction with CO depend on the CO surface coverage in a very nonlinear fashion. Translating the effect to the $N_2O$ + CO reaction results in $k_2$ and $k_3$ being given by

$$k_2 = \psi_2 k_2^0 \exp(-E_2/RT) \quad [20]$$

$$k_3 = \psi_3 k_3^0 \exp(-E_3/RT), \quad [21]$$

where $\psi_2$ and $\psi_3$ are the enhancement factors which are greater than unity (5 and 100, respectively) when the surface is in the (1 × 1) phase (high CO coverage). For the reconstructed (5 × 20) phase (low CO coverage), $\psi_2$ = 1 and $\psi_3$ = 1 always hold.

For intermediate coverage between $\theta_{CO}$ = 0.1 and $\theta_{CO}$ = 0.95, the values of $\psi_2$ and $\psi_3$ depend on the prior state of the surface as shown in Fig. 7 of Graham and Lynch (7), where it was assumed that the entire surface transforms into the (1 × 1) phase when the fractional CO surface coverage exceeds the critical value of 0.95 with the metal surface remaining in the (1 × 1) phase until the fractional CO surface coverage falls below the critical value of 0.1.

Graham and Lynch (7) used the same value of 250 for the enhancement factors for the (1 × 1) phase for both the surface reaction rate constant and the oxygen sticking probability. In this study a lower value of $\psi_2$ (=5) as compared to $\psi_3$ (=100) was sufficient to describe the high time-average CO conversions obtained during the feed cycling experiments. It would therefore appear that the rate enhancement for $N_2O$ dissociation due to hex ↔ (1 × 1) surface transition is much smaller than the increase of approximately two orders of magnitude for the oxygen sticking probability. This can be attributed to the differences in the adsorption mechanisms of $O_2$ and $N_2O$. In a study of comparative adsorption of $O_2$ and $N_2O$ on platinum-recrystallized ribbons using thermal desorption and mass spectrometry, Alnot *et al.* (41) noted that oxygen adsorption at 300 K leads to three binding states while $N_2O$ adsorption fills only the most energetic one. The sticking coefficient for $O_2$ dissociative adsorption at 500 K was found to be 0.16 as compared to $6.8 \times 10^{-3}$ for $N_2O$ dissociative adsorption. They attributed the differences between $O_2$ and $N_2O$ dissociative adsorption to steric factors. Daniel *et al.* (42) noted that for a clean Rh(100) surface, the saturation coverage of oxygen is twice as large for $O_2$ as $N_2O$. McCabe and Wong (2) attributed the lower rate of the CO + $N_2O$ reaction compared to CO + $O_2$ and CO + NO reactions under the conditions characterized by high CO surface coverage to the lower rate of dissociative adsorption of $N_2O$ as compared to the rate of dissociative $O_2$ and NO adsorption on alumina-supported Rh catalyst.

The time-average CO conversions were calculated by integrating Eqs. [5]–[9]. In the initial attempts to determine suitable model parameters, the values of $K_1$, $K_{-1}$, $K_2$, $K_3$, and $N_{CO}$ were chosen so that the model predictions matched the experimental CO conversions both for out-of-phase feed cycling (Fig. 4) and for the steady-state experiments at 499 K (Fig. 2). The model parameters were then further adjusted so as to describe not only the experimental data for all of the forced composition cycling experiments (Figs. 4, 6, and 8) but also the steady-state data from the earlier study (4). All integrations were carried out over several cycles until the CO conversions per cycle based on CO, $N_2O$, and $CO_2$ matched within 0.2% of each other and did not change more than 0.2% for two consecutive cycles. The percentage change in the fractional oxygen surface coverage was used as a criterion as given by

$$\left|\frac{\theta_O(n\tau_C) - \theta_O((n-1)\tau_C)}{\theta_O((n-1)\tau_C)}\right| \leq 10^{-3}, \quad n = 1, 2, 3, \ldots . \quad [22]$$

The model predictions for time-average CO conversions for out-of-phase cycling are shown by the solid line in Fig. 4. The initial slope of the conversion-frequency curve is strongly dependent on the ratio of the bulk volume to catalyst surface capacitances ($\alpha_m$) as demonstrated by Lynch (14). Therefore, the value of the catalyst adsorption capacity, $L_m$, was adjusted down from $2 \times 10^{-5}$ to $1.42 \times 10^{-5}$ mol/m$^2$, to match the predictions with the experimental data for the frequencies lower than 3 mHz. The other kinetic parameter values are listed in Table 1.

As can be seen from Table 1, different values of the parameters $K_{-1}$, $K_2$, $K_3$, and $N_{CO}$ were used for the two models. The parameter values for the CO self-exclusion model were selected so as to describe all of the steady-state multiplicity data from the earlier study (4). However, as shown in Fig. 4, this model fails to describe the high values of time-average CO conversions obtained during out-of-phase feed composition cycling. Any attempt to force the model predictions to match the out-of-phase feed cycling data led to significant model–experimental discrepancies for the steady-state multiplicity data.

The model parameters for the surface-phase transformation model have been chosen so as to describe both the dynamic and the steady-state experimental data. A comparatively low value of $N_{CO}$ = 1.0015 was necessary for the surface-phase transformation model because of the high enhancement (100 times) of the surface reaction rate for phase 2. Nevertheless the CO self-exclusion effect was still required in the model in order to describe the

unique low conversion steady-state data. The model predicts that above a critical frequency of 11 mHz no improvement in the time-average conversion can be obtained. This prediction is consistent with the experimental results which indicate a critical frequency in the range of 11.5 to 12.2 mHz. The time-average conversion predicted by the model is less than the experimental data by approximately 5% for frequencies greater than 7 mHz. However, the surface-phase transformation model is clearly superior to the CO self-exclusion model for describing the rate enhancement obtained during out-of-phase cycling in the intermediate frequency range of 2.5 to 11 mHz.

The surface-phase transformation model was also able to describe the steady-state multiplicity behavior from the earlier study (4) as shown in Fig. 2. The steady-state behavior at the other temperatures of 461, 480, and 520 K could also be predicted by the model assuming that the rate parameters follow an Arrhenius-type temperature dependency through the use of the values of the various activation energies given in Table 1. The activation energies used in Table 1 are within 30% of the values used to describe the steady-state behavior in the earlier study (4), where an extensive comparison with other experimental studies was made.

To predict the dynamic $CO_2$ response of the model, the effect of $CO_2$ adsorption–desorption on the alumina support was accounted for through the use of values of $K_4$ and $K_{-4}$ given under Notation. The model predictions for the dynamic $CO_2$ response for the out-of-phase cycling are shown by the solid lines in Fig. 3. It can be seen that excellent model–experimental agreement is achieved with only a slight mismatch occurring in a few locations. The time-average conversion calculated from the model for the out-of-phase cycling is shown by the solid curve in Fig. 4. It is seen that the model can describe the high time-average conversions in the intermediate-frequency range, something that was not possible to achieve with the other two models examined earlier.

The time-average conversions calculated from the model for 90° and 270° phase leads are shown in Fig. 6. The model predicts near 100% conversion for 90° phase lead in the frequency range of 4 and 7.8 mHz, which is approximately 10% higher than the experimental data. Otherwise, the model describes all of the other features of the conversion–frequency curve including the initial slope, the high conversions at intermediate frequencies and the critical frequencies which closely match the experimental results. Figure 7 shows a close model–experimental agreement for the dynamic $CO_2$ response at a frequency of 1.25 mHz.

It can be seen from Fig. 8 that the model can almost quantitatively describe the effect of $N_2O$ phase lead on the time-average conversion. The model predicts near 100% time-average conversion for a range of $N_2O$ phase leads at frequencies of 2, 5, and 7.04 mHz as shown in Figs. 8a, 8b, and 8c, respectively. In Fig. 8d, the model predictions are shown for a frequency of 11 mHz and these are qualitatively very similar to the experimental results at 11.11-mHz frequency, although the conversion imporovements are predicted only for a narrow range (176° to 180°) of phase leads. The model predicts no improvement in CO conversions for frequencies higher than 11 mHz. Figure 9 shows that the model predictions for the dynamic $CO_2$ response closely match the experimental results for the five frequencies.

The model predictions of near 100% time-average conversions, as shown in Figs. 6 and 9, suggest that a true global maximum in time-average conversion exists in the range of the frequencies and the phase leads corresponding to near 100% conversion predictions. The maximum time-average conversion can be predicted by optimizing the objective function

$$f_{TA} = \frac{100}{\tau_C} \int_0^{\tau_C} Z(\tau)\, d\tau. \qquad [23]$$

The constraints for the optimization are given by the ordinary differential equations [5]–[10]. Zolotarskii *et al.* (43) presented an analysis of a similar optimal periodic-control problem and observed that the optimal performance is attained when the two input cycles overlap to a certain extent, which is consistent with this study.

## CONCLUSIONS

The kinetic behavior of the $N_2O$ + CO reaction over an alumina-supported Pt catalyst has been examined using forced feed composition cycling experiments. The composition cycling strategies involved variation of the phase angle between the two square-wave cycles of CO and $N_2O$, respectively, in a manner similar to that used by Graham and Lynch (7) for CO + $O_2$ reaction. The time-average CO conversions during the cycling experiments were significantly higher than the steady-state conversion of 20% at 499 K. The maximum time-average conversion for the experiments with $N_2O$ phase leads of less than 180° were higher than the maximum conversion obtained during the out-of-phase cycling. In this study, the maximum conversion of 93.5% was obtained at a cycling frequency of 2 mHz at an $N_2O$ phase lead of 40°. The reaction rate enhancements were generally observed in the intermediate frequency range ($\omega < 11$ mHz), for an intermediate value of $N_2O$ phase lead. At cycling frequencies higher than 11 mHz, as well as for phase leads closer to 0° and 360°, the time-average conversion was very close to its steady-state value. These observations are similar to those made for the CO + $O_2$ reaction (7).

A kinetic model incorporating the two main features, namely, the adsorbate-induced (1 × 1) ↔ hex surface-phase transformation of Pt and the CO self-exclusion effect, has been proposed to describe the dynamic behavior including the high time-average conversion and the dynamic $CO_2$ response during cycling. The model is based on a reaction mechanism consisting of three elementary steps, namely, the reversible adsorption of CO, the irreversible dissociative adsorption of $N_2O$ to form adsorbed oxygen and gaseous $N_2$, and the reaction of adsorbed carbon monoxide and adsorbed atomic oxygen to produce gaseous $CO_2$. For a particular set of values of the kinetic parameters, the model could quantitatively describe the dynamic behavior during feed composition cycling, as well as the experimental steady-state multiplicity behavior of the reaction at other temperatures. Thus, this relatively simple model adequately describes a large amount of steady-state and dynamic data.

## APPENDIX: NOTATION

| | |
|---|---|
| $a_m$ | total surface area of supported catalyst, 9.4 $m^2$ |
| $a_s$ | total surface area of the support, 2092 $m^2$ |
| [CO] | reactor CO concentration, $mol/m^3$ |
| $[CO]_0$ | time-average feed CO concentration, $F_{CO}P/RT$, $mol/m^3$ |
| $[CO_2]$ | reactor $CO_2$ concentration, $mol/m^3$ |
| CO–M | adsorbed CO species on catalyst surface |
| $E_{-1}$ | activation energy for CO desorption, kJ/mol |
| $E_2$ | activation energy for $N_2O$ dissociation, kJ/mol |
| $E_3$ | activation energy for surface reaction, kJ/mol |
| $E_{-4}$ | activation energy for $CO_2$ desorption from the support, 83.1 kJ/mol |
| $F_{CO}$ | time-average mole fraction CO in feed |
| $F_{N_2O}$ | time-average mole fraction $N_2O$ in feed |
| $f_{TA}$ | time-average CO conversion, % |
| $k_1$ | CO adsorption rate constant, $6.87S_{CO}T^{0.5}/L_m$, $m^3/mol \cdot s$ |
| $k_{-1}$ | CO desorption rate constant, $k^0_{-1}\exp(-E_1/RT)$, $s^{-1}$ |
| $k^0_{-1}$ | CO desorption pre-exponential factor, $s^{-1}$ |
| $k_2$ | $N_2O$ dissociation rate constant, $\psi_2 k_2^0 \exp(-E_2/RT)$, $m^3/mol \cdot s$ |
| $k_2^0$ | $N_2O$ dissociation pre-exponential factor, $m^3/mol \cdot s$ |
| $k_3$ | surface reaction rate constant, $\psi_3 k_3^0 \exp(-E_3/RT)$, $m^2/mol \cdot s$ |
| $k_3^0$ | surface reaction pre-exponential factor, $m^2/mol \cdot s$ |
| $k_{-4}$ | $CO_2$ desorption rate constant, $k^0_{-4}\exp(-E_{-4}/RT)$, $s^{-1}$ |
| $k^0_{-4}$ | $CO_2$ desorption pre-exponential factor, 3.83 × $10^9$ $s^{-1}$ |
| $K_1$ | dimensionless CO adsorption rate constant, $a_m L_m k_1/Q_0$ |
| $K_{-1}$ | dimensionless CO desorption rate constant, $a_m L_m k_{-1}/Q_0[CO]_0$ |
| $K_2$ | dimensionless $N_2O$ dissociation rate constant, $a_m L_m k_2/Q_0$ |
| $K_3$ | dimensionless surface reaction rate constant, $a_m L_m^2 k_3/Q_0[CO]_0$ |
| $K_4$ | dimensionless $CO_2$ adsorption rate constant, $5.48S_{CO_2}a_s T^{0.5}/Q_0$ |
| $K_{-4}$ | dimensionless $CO_2$ desorption rate constant, $a_s L_s k_{-4}/Q_0[CO]_0$ |
| $L_m$ | adsorption capacity of platinum surface, $mol/m^2$ |
| $L_s$ | $CO_2$ adsorption capacity of the support, 1.2 × $10^{-6}$, $mol/m^2$ |
| $n$ | number of cycles |
| $N_{CO}$ | CO self-exclusion factor |
| $[N_2O]$ | reactor $N_2O$ concentration, $mol/m^3$ |
| $[N_2O]_0$ | time-average feed $N_2O$ concentration, $mol/m^3$ |
| O–M | adsorbed oxygen species on catalyst surface |
| $P$ | reactor pressure, 1.03 × $10^5$ Pa |
| $Q_0$ | feed volumetric flow rate at the reactor operating conditions, 1.11 × $10^{-8}$ $T$, $m^3/s$ |
| $Q_n$ | ratio of exit to feed volumetric flow rates |
| $R$ | gas constant, 8.314 $m^3 \cdot Pa/mol \cdot K$ |
| $S_{CO}$ | CO sticking probability on catalyst |
| $S_{CO_2}$ | $CO_2$ sticking probability on alumina support, 8.3 × $10^{-9}$ |
| $t$ | time, s |
| $T$ | reactor temperature, 499 K |
| $V$ | effective free volume of the reactor, 2.15 × $10^{-4}$ $m^3$ |
| $X$ | dimensionless reactor CO concentration, $[CO]/[CO]_0$ |
| $X_0$ | instantaneous dimensionless feed CO concentration (0 or 2 in this study) |
| $Y$ | dimensionless reactor $N_2O$ concentration, $[N_2O]/[N_2O]_0$ |
| $Y_0$ | instantaneous dimensionless feed $N_2O$ concentration (0 or 2 in this study) |
| $Z$ | dimensionless reactor $CO_2$ concentration, $[CO_2]/[CO]_0$ |
| $Z_0$ | instantaneous dimensionless feed $CO_2$ concentration (0 in this study) |
| $\alpha_m$ | ratio of bulk volume to metal surface capacitances, $[CO]_0V/a_mL_m$ (0.298 in this study) |
| $\alpha_s$ | ratio of bulk volume to support surface capacitances, $[CO]_0V/a_sL_s$ (0.024 in this study) |
| $\theta_{CO}$ | fractional CO surface coverage on platinum surface |
| $\theta_O$ | fractional oxygen surface coverage of platinum surface |
| $\xi_{CO_2}$ | fractional $CO_2$ surface coverage on the support surface |

$\tau$ dimensionless time based on the reactor residence time, $Q_0 t/V$
$\tau_c$ dimensionless cycle period, $Q_0/V\omega$
$\phi_{N_2O}$ $N_2O$ phase lead, degrees
$\psi_2$ enhancement factor for $N_2O$ dissociation, 1 for $(5 \times 20)$ phase and 5 for $(1 \times 1)$ phase
$\psi_3$ enhancement factor for surface reaction, 1 for $(5 \times 20)$ phase and 100 for $(1 \times 1)$ phase
$\omega$ frequency of cycling, $Q_0/V\tau_c$, Hz

## ACKNOWLEDGMENT

This work has been supported by the Natural Sciences and Engineering Research Council of Canada.

## REFERENCES

1. Cho, B. K., Shanks, B. H., and Bailey, J. E., *J. Catal.* **115,** 486 (1989).
2. McCabe, R. W., and Wong, C., *J. Catal.* **121,** 422 (1990).
3. Muraki, H., and Fujitani, Y., *Ind. Eng. Chem. Prod. Res. Dev.* **25,** 414 (1986).
4. Sadhankar, R., Ye, J., and Lynch, D. T., *J. Catal.* **146,** 511 (1994).
5. Kobayashi, M., *in* "Chemical Reaction Engineering—Boston" (J. Wei and C. Georgakis, Eds.), ACS Symposium Series, Vol. 176, p. 213. ACS, Washington, DC, 1981.
6. Graham, W. R. C., and Lynch, D. T., *AIChE J.* **33,** 792 (1987).
7. Graham, W. R. C., and Lynch, D. T., *AIChE J.* **36,** 1796 (1990).
8. Bailey, J. E. *in* "Chemical Reactor Theory: A Review" (L. Lapidus and N. R. Amundson, Eds.), p. 758. Prentice-Hall, Englewood Cliffs, NJ, 1977.
9. Cutlip, M. B., *AIChE J.* **25,** 502 (1979).
10. Cutlip, M. B., Hawkins, C. J., Mukesh, D., Morton, W., and Kenney, C. N., *Chem. Eng. Commun.* **22,** 329 (1983).
11. Zhou, X., Barshad, Y., and Gulari, E., *Chem. Eng. Sci.* **41,** 1277 (1986).
12. Cho, B. K., *Ind. Eng. Chem. Fundam.* **22,** 410 (1983).
13. Lynch, D. T., *Can. J. Chem. Eng.* **61,** 183 (1983).
14. Lynch, D. T., *Can. J. Chem. Eng.* **62,** 601 (1984).
15. Graham, W. R. C., and Lynch, D. T., *in* "Catalysis 1987—Proceedings of the Tenth North American Meeting of the Catalysis Society, San Diego, 1987)" (J. M. Ward, Ed.), Studies in Surface Science and Catalysis, Vol. 38, p. 693. Elsevier, Amsterdam, 1988.
16. Vaporciyan, G., Annapragada, A., and Gulari, E., *Chem. Eng. Sci.* **43,** 2957 (1988).
17. Prairie, M. R., Cho, B. K., Oh, S. H. Shinouskis, E. J., and Bailey, J. E., *Ind. Eng. Chem. Res.* **27,** 1396 (1988).
18. Lynch, D. T., Emig, G., and Wanke, S. E., *J. Catal.* **97,** 456 (1986).
19. Heilmann, P., Heinz, K., and Müller, K., *Surf. Sci.* **83,** 487 (1979).
20. McCarroll, J. J., *Surf. Sci.* **53,** 297 (1975).
21. Helms, C. R., Bonzel, H. P., and Kelemen, S., *J. Chem. Phys.* **65,** 1773 (1976).
22. Bonzel, H. P., and Pirug, G., *Surf. Sci.* **62,** 45 (1977).
23. Norton, P. R., Davies, J. A., Creber, D. K., Sitter, C. W., and Jackman, T. E., *Surf. Sci.* **108,** 205 (1981).
24. Behm, R. J., Thiel, P. A., Norton, P. R., and Ertl, G., *J. Chem. Phys.* **78,** 7437 (1983).
25. Gardner, P., Tüshaus, M., Martin, R., and Bradshaw, A. M., *Surf. Sci.* **240,** 112 (1990).
26. Barteau, M. A., Ko, E. I., and Madix, R. J., *Surf. Sci.* **102,** 99 (1981).
27. Thiel, P. A., Behm, R. J., Norton, P. R., and Ertl, G., *J. Chem. Phys.* **78,** 7448 (1983).
28. Pirug, G., Brodén, G., and Bonzel, H. P., *in* "Proceedings of the Seventh International Vacuum Congress and the Third International Conference on Solid Surfaces, Vienna, 1977" (R. Dobrozemsky, F. Rüdenauer, F. P. Viehböck, and A. Berth, Eds.), p. 907. International Union for Vacuum Science Technique and Application, 1977.
29. Bonzel, H. P., Brodén, G., and Pirug, G., *J. Catal.* **53,** 96 (1978).
30. Ertl, G., Norton, P. R., and Rüstig, J., *Phys. Rev. Lett.* **49,** 177 (1982).
31. Schwartz, S. B., and Schmidt, L. D., *Surf. Sci.* **183,** L269 (1987).
32. Schwartz, S. B., and Schmidt, L. D., *Surf. Sci.* **206,** 169 (1988).
33. Sales, B. C., Turner, J. E., and Maple, M. B., *Surf. Sci.* **114,** 381 (1982).
34. Kurtanjek, Ž., and Froment, G. F., *Chem. Eng. Sci.* **40,** 3189 (1991).
35. Yeates, R. C., Turner, J. E., Gellman, A. J., and Somorjai, G. A., *Surf. Sci.* **149,** 175 (1985).
36. Burrows, V. A., Sundaresan, S., Chabal, Y. J., and Christman, S. B., *Surf. Sci.* **180,** 110 (1987).
37. Collins, N. A., Sundaresan, S., and Chabal, Y. J., *Surf. Sci.* **180,** 136 (1987).
38. Dagonnier, R., Dumont, M., and Nuyts, J., *J. Catal.* **66,** 130 (1980).
39. Schüth, F., and Wicke, E., *in* "Instationary Processes and Dynamic Experimental Methods in Catalysis, Electrochemistry and Corrosion" (G. Sandstede and G. Kreysa, Eds.), Dechema Monogr., Vol. 120, p. 429. Dechema, Frankfurt-am-Main, 1989.
40. Wang, T., Lee, C., and Schmidt, L. D., *Surf. Sci.* **163,** 181 (1985).
41. Alnot, M., Cassuto, A., Fusy, J., and Pentenero, A., *Jpn. J. Appl. Phys. Suppl.* **2**(2), 79 (1974).
42. Daniel, W. M., Kim, Y., Peebles, H. C., and White, J. M., *Surf. Sci.* **111,** 189 (1981).
43. Zolotarskii, I. A., Bogdashev, S. M., and Matros, Yu. Sh., *React. Kinet. Catal. Lett.* **37,** 43 (1988).